



**HAL**  
open science

## **Aerodynamic analysis of 3D multi-elements wings : an application to wingsails of flying boats**

Alessandro Fiumara, Nicolas Gourdain, Vincent Chapin, Julien Senter

► **To cite this version:**

Alessandro Fiumara, Nicolas Gourdain, Vincent Chapin, Julien Senter. Aerodynamic analysis of 3D multi-elements wings : an application to wingsails of flying boats. Royal Aeronautical Society, 2016 Applied Aerodynamic Conference, Jul 2016, Bristol, United Kingdom. pp.1-12. hal-02168475

**HAL Id: hal-02168475**

**<https://hal.science/hal-02168475>**

Submitted on 28 Jun 2019

**HAL** is a multi-disciplinary open access archive for the deposit and dissemination of scientific research documents, whether they are published or not. The documents may come from teaching and research institutions in France or abroad, or from public or private research centers.

L'archive ouverte pluridisciplinaire **HAL**, est destinée au dépôt et à la diffusion de documents scientifiques de niveau recherche, publiés ou non, émanant des établissements d'enseignement et de recherche français ou étrangers, des laboratoires publics ou privés.



## Open Archive Toulouse Archive Ouverte (OATAO)

OATAO is an open access repository that collects the work of some Toulouse researchers and makes it freely available over the web where possible.

This is an author's version published in: <https://oatao.univ-toulouse.fr/23770>

### To cite this version :

Fiumara, Alessandro and Gourdain, Nicolas and Chapin, Vincent and Senter, Julien Aerodynamic analysis of 3D multi-elements wings : an application to wingsails of flying boats. (2016) In: Royal Aeronautical Society, 2016 Applied Aerodynamic Conference, 19 July 2016 - 21 July 2016 (Bristol, United Kingdom).

Any correspondence concerning this service should be sent to the repository administrator:

[tech-oatao@listes-diff.inp-toulouse.fr](mailto:tech-oatao@listes-diff.inp-toulouse.fr)

# AERODYNAMIC ANALYSIS OF 3D MULTI-ELEMENTS WINGS: AN APPLICATION TO WINGSAILS OF FLYING BOATS

Alessandro Fiumara<sup>1</sup>, Nicolas Gourdain<sup>2</sup>, Vincent Chapin<sup>3</sup>, Julien Senter<sup>4</sup>

## Nomenclature

$\alpha$	Angle of attack
$\gamma$	Intermittency factor
$\delta$	Flap deflection angle
$\delta_{BL}$	Boundary layer thickness
$c$	Chord
$c_1$	Main element chord
$c_2$	Flap chord
$C_D$	Drag coefficient
$C_L$	Lift coefficient
$g$	Gap dimension of the slot
$H$	Wingsail height
$k$	Turbulent kinetic energy
<i>ISAE</i>	Institut Supérieur de l'Aéronautique et de l'Espace
$l$	Local distance from the wing surface
<i>L.E.</i>	Leading Edge
$o$	Overlap dimension of the slot
<i>PIV</i>	Particule Image Velocimetry
<i>RANS</i>	Reynolds Averaged Navier Stokes
$Re$	Reynolds number
$Re\vartheta$	Momentum thickness Reynolds number
<i>T.E.</i>	Trailing Edge
$U$	x velocity component
$U_e$	Velocity external to the viscous layers
$V$	Velocity magnitude
<i>WT</i>	Wind Tunnel (experimental)
$x, y, z$	Axes of the wingsail reference system
$x_{rot}$	Position of the rotation axis of the flap
$x_v, y_v, z_v$	Axes of the wind tunnel reference system
$y_F$	y distance of flap L.E.
$y^+$	Dimensionless wall distance
$z^*$	Normalized height position z/H

## 1. Introduction

Since the beginning of aeronautics, the two-element wing also known as slotted flap design was introduced on the aircraft to improve the high-lift capabilities in case of take-off and landing compared to simple flapped wing design. This same two-element design has been recently transposed on the naval wing, the “wingsail”, used to propel the “America’s Cup” catamaran (Fig. 1) instead of the soft mainsail. This rig is constantly set to flap deflection angles

varying from 15° to 40° and the slotted configuration helps in increasing its lift performances. After its introduction in the naval domain, the wingsail has enhanced the yacht performances in both upwind and downwind conditions. Nevertheless the abrupt stall characteristics of the wing make difficult its management bringing to spectacular and hard capsizes.



**Fig. 1 - America’s Cup catamaran propelled with two-element wingsail.**

The wingsail geometry is made of a main element and a flap, divided by a slot that cannot be adjusted in size. The airfoils are symmetric for both the elements in a way to allow the wingsail to tack on both the yacht sides. The flap can be only rotated on its axis located near the main trailing edge. The size in chord is equally distributed between the main element and the flap. Because of these geometric constraints, the research of the configuration that optimizes the high-lift wing performances is more complex compared to an aeronautic wing. Furthermore the analysis is also made hard by the flow conditions characterised by the unsteadiness of the sea environment and the velocity gradients due to the sea boundary layer.

The high-lift wing configurations were largely studied in the years in order to improve the lift possibilities of the aeronautical wings. Particular attention was devoted to the research of the optimal slot characteristics (Woodward et al. [1], Wentz et al. [2]). Indeed, the jet of the slot allows enhancing the wing performance but only if the slot size is correctly adjusted [3]. For the wingsail case the studies realized are not numerous and rarely dealt with 3D test cases. One of them is the experimental campaign made by Turnock et al. [4] on a 3D scale model of C-class catamaran but a slot analysis was not included in the analysis. One experimental campaign focused on the slot influence on the

wingsail performance is the one performed by Blakeley et al. [5] on a two-element airfoil of AC 45 wingsail. Nevertheless this study did not fulfil all the flap deflection angle settings but considering only low cambered configurations of the wingsail. Haack [6] went further investigating also high cambered configurations by numerical simulations on a class-C wingsail. Chapin et al. also analysed the role of the slot jet in the wingsail high-lift capabilities performing numerical studies on an AC 72 scale model wingsail. They deepened the slot influence not only on the aerodynamic coefficients but also on the stall evolution of the wing.

The works exposed in this paper are the continuation of the analyses of Chapin et al. [7]. A wind tunnel campaign was performed the AC 72 wingsail at different operating points (variation in angle of attack and flap deflection angle). The aerodynamic coefficients were extracted and in particular the flow physics was analysed by viscous oil visualizations, PIV analysis and flow cones tests. Contemporarily a numerical study was also performed on the same wingsail scale model to enlarge the slot test cases. The aim of this study is to obtain an exhaustive description of the flow physics of the slot and its influence on the wingsail performance and stall characteristics. The results of the analysis can be also helpful to improve the wing design of light aircraft to prevent dangerous abrupt stall conditions especially during the landing condition when the flap is normally high deflected. The similarity in geometry between the aeronautical and the naval wing together with the relative low speeds of light aircraft make the two rigs comparable.

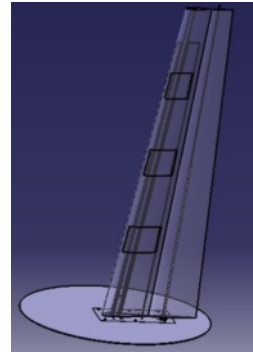
## 2. Wind Tunnel Tests

### 2.1 Experimental methodology

A wingsail scale model of the America's Cup class AC 72 was designed and used for the tests (Fig. 2). It is composed of two elements, the main element and the flap, divided by a slot through which the air can flow. The flap can be set at on two different angles ( $\delta=15^\circ$  and  $\delta=25^\circ$ ), pivoting on its axis located at 95% of the main axis. The slot size can be adjusted at 6 mm ( $g/c_l=2.4\%$ ) and 12 mm ( $g/c_l=4.8\%$ ). The two elements are composed by NACA symmetrical airfoils, to allow wingsail tacking from both sides.

The wind tunnel used for the experimental campaign is the S4 facility owned by "Institut Supérieur de l'Aéronautique et de l'Espace" ISAE-Supaero in Toulouse. It is an open return wind tunnel with open test section (Fig. 3). The vein has an elliptical shape of 3m×2m. The flow is created by

the aspiration created by three fan drives of 90kW each, located at the end of the diffuser (st.5 in fig.3). The maximum speed in the duct is 42 m/s. To eliminate low frequency oscillations inside the duct (inherent to such open loop configurations), a gap was created in the first section of the diffuser (st. 4). In this way, the oscillations are dumped by the creation of a secondary flow, exterior to the diffuser, recirculating from the gap to the intake of the diffuser itself (st. 3).



$$H = 1.8 \text{ m}$$

$$Re_{root} = 6.4 \times 10^5$$

$$Re_{tip} = 2.9 \times 10^5$$

$$g = 6 \text{ mm}$$

$$x_{rot}/c_l = 95\%$$

Fig. 2 - Geometry of the wingsail with its main parameters.



$$\text{vein shape: elliptical}$$

$$\text{vein section: } 3\text{m} \times 2\text{m}$$

$$\text{vein length: } 2 \text{ m}$$

$$V_{max}: 42 \text{ m/s}$$

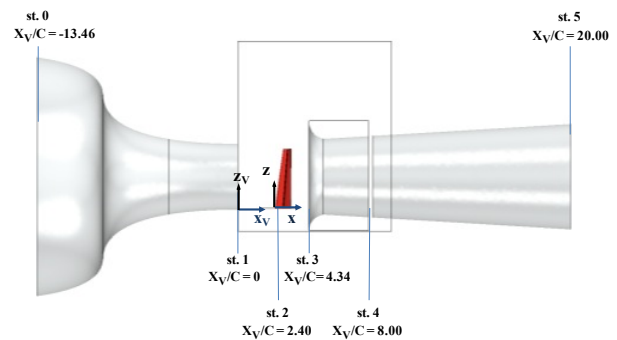


Fig. 3 - Scheme of the S4 wind tunnel facility and main parameters.

The wingsail model was mounted vertically in the vein (st.2) on a rotating plate that allows adjusting the angle of attack. To reduce the interactions between balance and the wingsail, a disk platform is posed at the base of the wing scale model.

The aerodynamic forces were estimated with a six-component balance. The maximum loads bearable by the

balance are 240 daN for the longitudinal force, 300 daN for the transversal force and 50 daNm for the heeling and the pitching moments. The aerodynamic forces were measured from a minimum angle of attack of  $-7^\circ$  to a maximum one of  $20^\circ$  with a step of  $0.5^\circ$ . Both the increasing and the decreasing paths were measured during the tests.

PIV 2D measurements were performed on the three reference section on the wingspan ( $z^*=0.25, 0.50, 0.75$ ) at different flap deflection angles and different angles of attack. The flow particles were lighted with a pulse laser with a pulse time of 3-5 ns and a maximum energy of 100 mJ. The flow images were taken by a HD camera ( $4008 \times 2672$  px) with an acquisition frequency of 2 Hz.

In fig. 3 the two reference systems used in this paper have been reported. The first one is the vein system  $(x_v, y_v, z_v)$ , whose origin is located at the end of the convergent section in correspondence to the symmetry plane of the vein and at the bottom of the convergent. The x-axis is the convergent-diffuser direction while the z-axis is directed upwards. The wingsail reference system  $(x, y, z)$  is translated to the previous one in a way that the origin is located on the leading edge of the wing root section, keeping its position in the symmetry plane of the vein ( $x=x_v+2.4c$ ,  $y=y_v$ ,  $z=z_v+0.022H$ ).

## 2.2 Flap deflection angle influence on lift

The experimental lift curves were reported in fig. 4 for the wingsail with slot  $g/c_1=2.4\%$  in both the low and high cambered configurations (i.e.  $\delta=15^\circ$  and  $\delta=25^\circ$ ).

As expected the effect in increasing the flap deflection angle is to move the lift curve toward highest lift coefficients keeping the same slope. However this effect can be observed for angles of attack lower than  $1^\circ$ . The increase in camber leads to a modification of the stall behavior of the wing and hence to a reduction of the lift performance of the wing at high angles of attack. This is true for the  $\delta=25^\circ$  case where the lift path curve appears fragmented. It presents two distinguished linear zones, from  $-7^\circ$  to  $1^\circ$  and to  $2^\circ$  to  $10^\circ$ , and four stall points, at  $1^\circ$ ,  $9^\circ$ ,  $12^\circ$  and  $17^\circ$ . The first stall, at  $\alpha=1^\circ$ , brings to an abrupt loss of 0.2 in  $C_L$ . The same characteristic can be observed for the second stall, at  $\alpha=9^\circ$ , but with a lower loss in lift. Between these two stalls the lift continues to increase linearly but with a smaller slope compared to the first linear path. Between  $10^\circ$  and  $12^\circ$  the lift has its last increasing path; it turns to gradually decrease up to  $17^\circ$  when the abrupt stall finally occurs.

In turn the low cambered case,  $\delta=15^\circ$ , the lift path shows the conventional wing characteristics when the angle of attack is increased: after a linear zone a stall occur at  $\alpha_{stall}=10^\circ$ . The final abrupt stall occurs at the same angle of attack for both the wing configurations at the same  $C_{Lmax}$ .

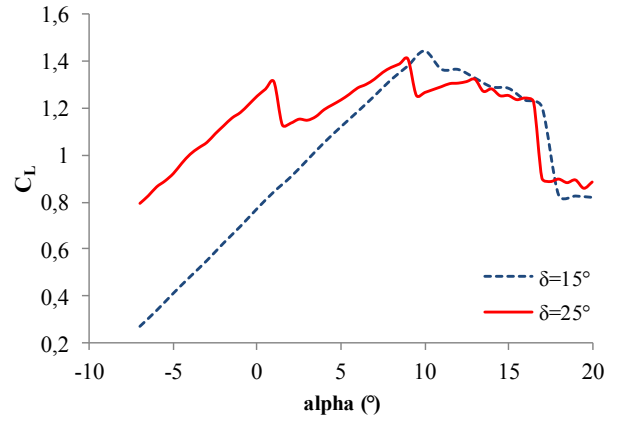


Fig. 4 -  $C_L$ - $\alpha$  curves for the wingsail in the  $g/c_1=2.4\%$  configuration at  $\delta=15^\circ$  and  $\delta=25^\circ$ .

## 2.3 Flow separation along the wingspan

The extents of the separated regions at different angles of attack were carried out from the flow cones tests performed during the wind tunnel campaign. These regions were reported in fig. 5 for the wingsail in the  $g/c_1=2.4\%$  slot case in both the low and the high flap deflection angle.

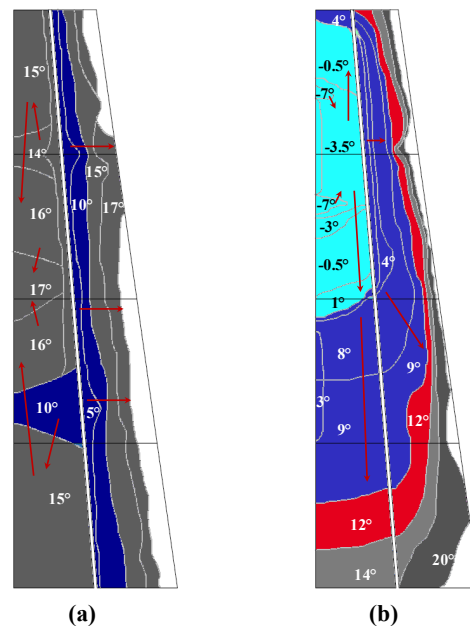


Fig. 5 - Maps of separated flow on the wingsail surface at different angles of attack in the  $g/c_1=2.4\%$  case at  $\delta=15^\circ$  (a) and  $\delta=25^\circ$  (b).

On the low cambered case, the flow starts to separate at  $\alpha=5^\circ$  on the main surface near the T.E. (Fig. 5(a)). At the stall angle of attack, i.e.  $\alpha=10^\circ$ , the extent of the separated zone includes the aft quarter chord region on the main and a zone on the flap at  $z^*=0.3$  due to the contamination of the flap hinge situated at  $z^*=0.39$ . Increasing the angle of attack, the separated zone on the main enlarges in the upstream direction up to the half of the chord. At  $\alpha=15^\circ$  separation starts to involve the flap surface, at first on the low sections and then enlarging on the entire wingspan.

The final abrupt stall observed in the  $C_L$  path, at  $\alpha=17^\circ$ , is caused by the flow separation from the maximum thickness section of the main element.

On the high cambered configuration (Fig. 5(b)), the multistep stall observed on the lift curve is caused by the flow separation not equally distributed throughout the wingspan. When the first stall occurs, at  $\alpha=1^\circ$ , the flow separates from the mid-high flap surface decreasing the flap effectiveness. As a consequence, the lift curve moves down as if an instantaneous reduction of the flap deflection angle was introduced. The flow separation from the main element surface in neighbors of the T.E. is the reason of the slope reduction of the second linear path, between  $\alpha=2^\circ$  and  $\alpha=9^\circ$ . This separation involves the sections on the wingspan where the flow is already separated on the flap. At  $\alpha=9^\circ$ , the propagation of the separated zone on the lower flap surface leads to an abrupt loss in flap effectiveness and hence to the occurring of the second stall.

The further increase in angle of attack provokes the enlargement of the separated zone downwards on the flap section and in the upstream direction on the main element. When the third stall occurs, at  $\alpha=12^\circ$ , the entire flap surface except a small region near the wing root is separated. The separated zone involves also the rear part of the main surface up to its maximum thickness section. The final abrupt stall at  $\alpha=17^\circ$  is caused as in the previous case by the lost of the maximum thickness section on the main.

To resume the difference behavior of the two wing configuration the following statement can be reported:

- $\delta=15^\circ$ : the separation evolves similarly on the entire wingspan. The flow starts to separate on the main T.E. for then enlarging on the flap and on the remaining main surface.
- $\delta=25^\circ$ : an asymmetric separation exists on the wingspan. The flow separates on the flap at first without involving directly the flow on the main. On the main the separation occurs only in a second time.

## 2.4 Flow separation on a wingsail section

To deepen the flow separation mechanism process already described in the previous section, the flowfield on a wingsail section was analyzed. The flowfield measurements were obtained from the PIV database. In fig. 6 and fig. 7 the velocity scalar maps were reported for the wing section at  $z^*=0.5$  for the low and high cambered wingsail configuration ( $g/c_1=2.4\%$ ).

For the  $\delta=15^\circ$  case, at  $\alpha=0^\circ$ , the flow is separated only on a small region near the main T.E. The jet of the slot lies on the flap surface in the neighbors of its L.E. interacting with the main wake (Fig. 6). With the increase of the angle of attack, at  $\alpha=10^\circ$ , the jet tends to move away from the flap surface and the extension of the separated zone on the main element enlarges. As a consequence the main wake is convected farther from the flap surface reducing the strength of its interaction with the jet of the slot. The flow on the flap surface is still kept attached. A further increase of the angle of attack gives raise to the contemporarily flow separation on both the main and the flap surface.

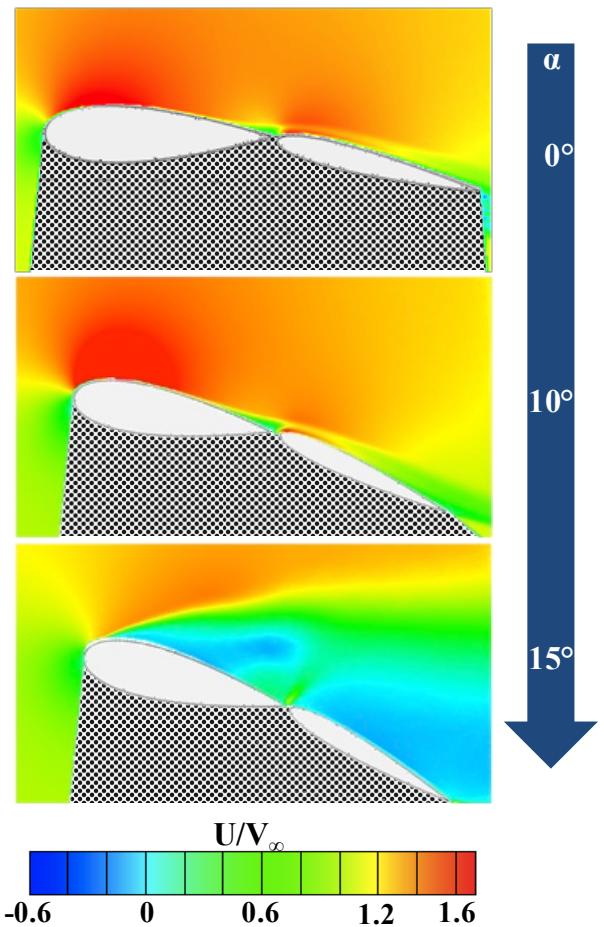


Fig. 6 – Velocity scalar maps on the  $z^*=0.5$  wingsail section for the  $g/c_1=2.4\%$ ,  $\delta=15^\circ$  case ( $\alpha=0^\circ$  -  $\alpha=10^\circ$  -  $\alpha=15^\circ$ ).

On the  $\delta=25^\circ$  configuration (Fig. 7), flow separation evolves independently on the two wingsail elements. At  $\alpha=0^\circ$ , the flow is separated on the aft half of the flap chord and on a small region near the main T.E. The jet of the slot does not lie on the flap surface. Increasing the angle of attack the flow separates entirely on the flap surface. The slot jet moves away from the flap surface and the separated region on the main element enlarges. The main wake flows far away from the flap surface reducing the interaction with the jet that tends to be lesser and lesser deviated increasing again the recirculation zone on the main. In this case the jet acts to separate the flow on the two elements preventing the abrupt stall of the main element when the flow is completely separated from the flap surface. Hence even in case of large flap separation the jet “filters” the downstream perturbations that are not felt by the main element. Furthermore for a range of  $8^\circ$  in angle of attack, from  $0^\circ$  to  $8^\circ$ , the flow appears substantially frozen.

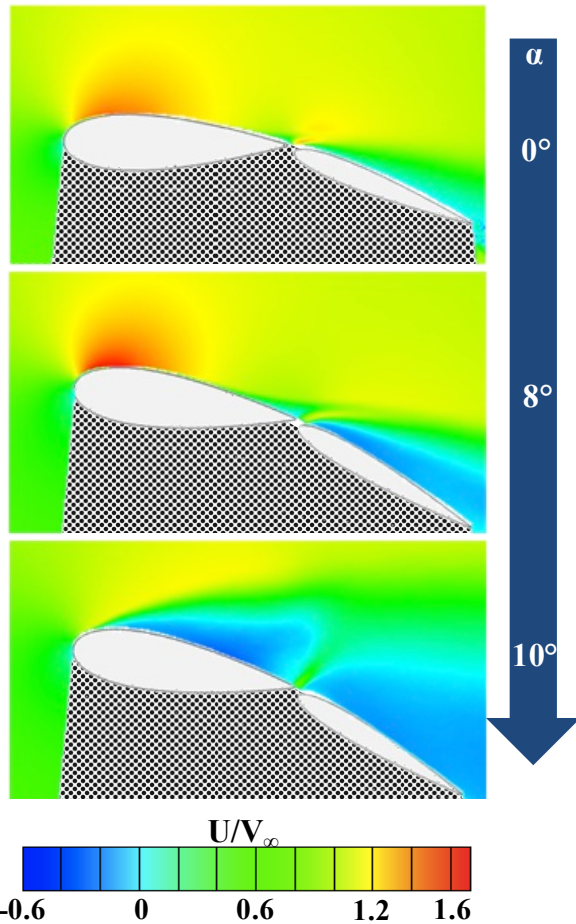


Fig. 6 – Velocity scalar maps on the  $z^*=0.5$  wingsail section for the  $g/c_1=2.4\%$ ,  $\delta=25^\circ$  case ( $\alpha=0^\circ$  -  $\alpha=8^\circ$  -  $\alpha=10^\circ$ ).

The stall characteristics of the wingsail are linked to the different operating point of the jet that is strictly dependent on the geometric features of the slot. Up to now the slot size

was characterized by the gap ( $g$ ) that in this paper is considered as the distance between the main T.E. and the flap L.E. when the flap is not deflected. Nevertheless the slot size is generally described by two parameters (Fig. 8): the overlap ( $o$ ) (the longitudinal distance between the main T.E. and the flap L.E.) and the  $y_F$  (the transversal distance between the main T.E. and the flap L.E.). The overlap assumes negative values when the main and the flap L.E. does not lie under the main element.

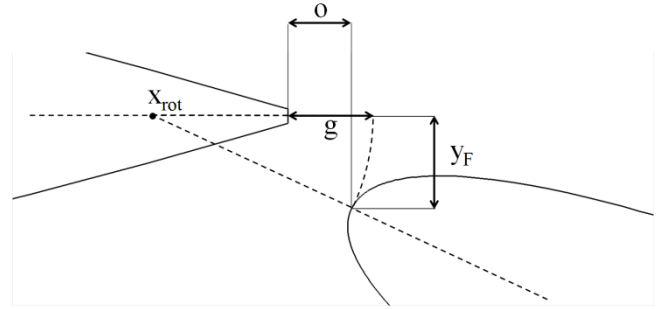


Fig. 8 – Slot parameters: gap ( $g$ ), overlap ( $o$ ), transversal distance ( $y_F$ ).

Because of the flap rotating mechanism, the overlap and the  $y_F$  are linked to the gap and to the flap deflection angle. For a fixed  $g$ , the more the flap is deflected the more the overlap and the  $y_F$  tend to increase. The actual slot size is hence strictly dependent on the flap deflection angle explaining the different behavior existing at the two flap deflection angles. The slot influence on the wingsail performance is then deeply analyzed in the next section.

## 2.5 Influence of slot variation

The wingsail configurations described in the previous section has the same gap ( $g$ ) of the slot, fixed at  $2.4\%$  of the root chord. To better investigate the slot influence on the wing performance, the  $C_L$  coefficient was measured for both the flap deflection angles modifying the gap size. The  $g$  was at first blocked with aluminum tape and then enlarged at  $4.8\%c_1$ .

In the low cambered configuration ( $\delta=15^\circ$ ), a slot reduction enhances the lift capabilities of the wing moving the curves toward higher lift values. The blocked configuration has the best performances up to  $\alpha=5^\circ$  for then assuming lift values comparable with the ones of the  $g/c_1=2.4\%$  case. Furthermore the blocked slot retards the occurring of the first stall, at  $\alpha=12^\circ$  instead of  $\alpha=10^\circ$ , but anticipate the final abrupt loss in lift ( $\alpha=15^\circ$  instead of  $\alpha=17^\circ$ ). In the largest slot case the  $C_{L,max}$  is  $17\%$  lower compared to the  $g/c_1=2.4\%$  configurations. This large loss in lift at high angles of attack is caused by an excessive downstream flap movement [1].

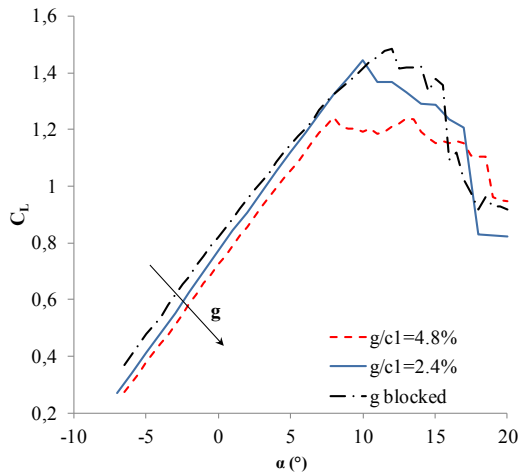


**Fig. 9** –  $C_L$  paths for  $\delta=15^\circ$  case at three gap sizes: blocked,  $g/c_1=2.4\%$ ,  $g/c_1=4.8\%$ .

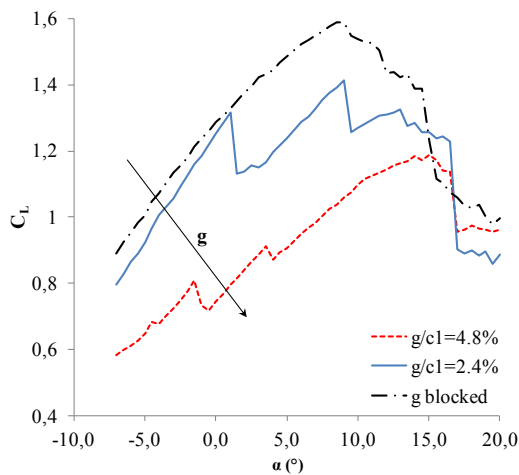


**Fig. 10** –  $C_L$  paths for  $\delta=25^\circ$  case at three gap sizes: blocked,  $g/c_1=2.4\%$ ,  $g/c_1=4.8\%$ .

The slot reduction enhances also the lift capabilities of the wing at high flap deflection angles. The blocked slot does not have the multistep behavior observed for the nominal case. The slope of the linear zone is lower than the one of the  $g/c_1=2.4\%$  case, but it continues to increase up to  $\alpha=9^\circ$  (i.e. in correspondence of the second stall of the nominal configuration). The lift reduces then slowly up to  $14^\circ$  after which an abrupt loss in lift occurs. A larger slot configuration spoils the performance of the wing with a difference of even 0.5 in lift coefficient. The final abrupt stall occurs at the same angle of attack of the nominal case.

### 3 Numerical analysis

Numerical simulations were performed on the wingsail scale model to deepen the investigation of the slot influence on further slot configurations that could not be examined by experimental means. The nominal wingsail configuration ( $g/c_1=2.4\%$ ) was at first simulated and compared to wind tunnel data in both the low and high cambered cases. Further numeric simulations were then performed, at both  $\delta=15^\circ$  and  $\delta=25^\circ$ , reducing the slot size at  $g/c_1=1.6\%$  and  $g/c_1=0.8\%$ .

#### 3.1 Numerical Methodology

To perform the numerical simulations the wingsail geometry was numerically reproduced in both the low and high flap deflection angle settings. The interface disk at the wing root was also modeled.

To correctly match the experimental results the wind tunnel geometry had to be also reproduced. The problem of the interaction of a high-lift configuration with the walls of a wind tunnel is a well known problem as already observed by Rogers et al. (2001) [8] and Nayani et al. (2015) [9]. The entire S4 facility was modeled reproducing also the entire room test. The process of the S4 wind tunnel modeling was exposed by Fiumara et al. (2015) [10].

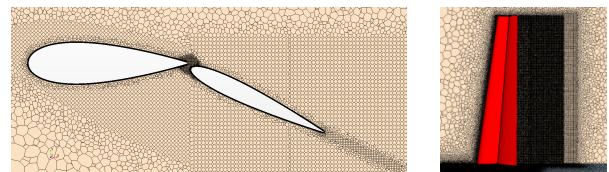


**Fig. 11** – Polyhedral mesh of the wingsail in the wind tunnel domain.

The wingsail was placed in the facility domain at station 2 (Fig. 3) as in the real case.

Because of the low Reynolds number ( $Re=4 \times 10^5$ ), the transition effects have also been considered by the use of the transition model  $\gamma-Re\theta$  proposed by Menter et al. (2004) [11][12], based on two transport equations modeling the intermittency factor  $\gamma$  and  $Re\theta$  in turbulent  $k\omega$ -SST model. The entire domain was meshed using Star-CCM+ with polyhedral (Fig.11). Prism layers were added on the wingsail, on the disk and on the wind tunnel convergent surface and set in a way to achieve a normalized distance to the wall  $y^+$  below 0.5 (Fig. 12) on the wingsail and below 20 on the convergent surface

The choice of a low wall  $y^+$  on the wingsail surface derives from the validation tests that had shown the sensitivity of the  $\gamma$ - $Re\theta$  model to the near wall discretization. In the validation tests for the transitional model developed by Suluksna et al. (2009) [13] (the one implemented in STAR-CCM+), Malan et al. (2009) [14] refers, for the high lift case, to a  $y^+$  at wall ranging from 0.1 to 0.8.

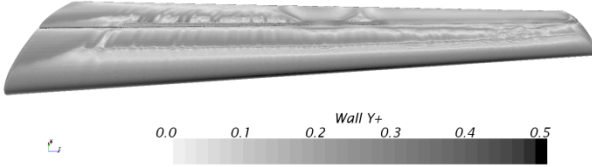


**Fig. 12** Scalar map on the wingsail upper surface, colored with the normalized distance to the wall  $y^+$ .

The mesh was refined particularly in the slot between the two elements of the wingsail and in wake region. Refinement was imposed also on the shear layers of the border of the vein. The final mesh counts 32 millions cells.

RANS simulations were run with a  $k-\omega$  SST turbulence model and activating the  $\gamma$ - $Re\theta$ . The pressure inlet and outlet boundary conditions were the same as imposed to the empty wind tunnel simulation in a way to keep a flow velocity at 20 m/s in the vein.

A first convergence was obtained on the aerodynamic coefficient after 4000 iterations. At the same time the pressure distribution over the wingsail and particularly the transition and the laminar bubble zones still presented strong oscillations caused by the unsteady characteristics of the transition phenomena. For this reason the RANS simulations were completed using an unsteady RANS approach, for a total time of 0.5 s using a  $2 \times 10^{-3}$  s time step, corresponding to 30 through flow times (the time needed for a particle to move from the leading edge to the trailing edge).

### 3.2 Numerical Validation

Numerical aerodynamic coefficients were extracted at different angles of attack and compared with the experimental data for the  $g/c_l=2.4\%$  setting.

At  $\delta=15^\circ$  the numerical simulation has the tendency to overestimate the  $C_L$  compared to the experimental data (Table 1). The difference in estimation is whatever less than 9%. URANS simulation predict an earlier stall that occurs between  $8^\circ$  and  $9^\circ$  while in the experimental case

stall occurs later at  $10^\circ$ . In fig. 12 the comparison of the skin friction features were reported. The transition is correctly detected on the main element as well as the laminar separation bubble even if its length is overestimated by the transitional model. On the flap the transitional model predicts a laminar zone on the first 30% of the chord that was not observed in the experimental tests. Indeed the transition detection is based on the reference magnitude in turbulent kinetic energy ( $k$ ) extracted at the upstream of the wing. This reference value is not adapted for the transition modeling on the flap surface where the flow convected from the main wake has a higher  $k$  magnitude.

**Table 1** –  $C_L$  comparison between experimental measurements and numerical simulations for  $\delta=15^\circ$ ,  $g/c_l=2.4\%$ .

	WT	WT (hyst.)	URANS	$\Delta$ URANS / WT	$\Delta$ (URANS/ WT (hyst.))
$\alpha=0^\circ$	0.77	0.77	0.85	+9.4%	+9.4%
$\alpha=8^\circ$	1.32	1.32	1.40	+5.7%	+5.7%
$\alpha=10^\circ$	1.45	1.12	1.41	-2.8%	+2.1%

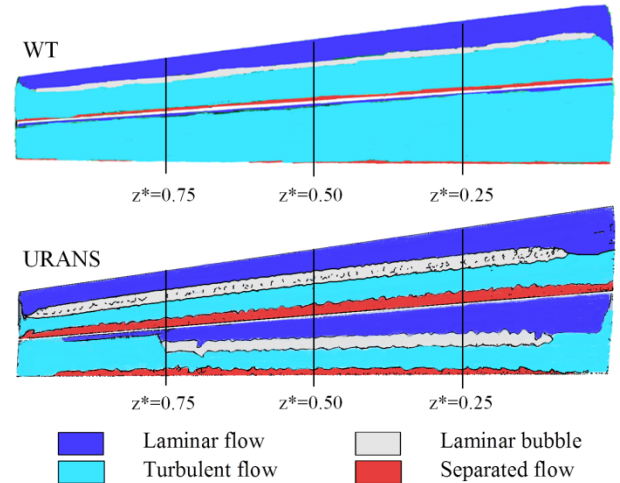


**Fig. 12** – Skin friction comparison between experimental viscous oil tests (top) and RANS simulation (bottom) for  $\delta=15^\circ$  and  $\alpha=0^\circ$ .

On the high cambered configuration of the wingsail the lift coefficient is estimated with an error of less than 5% for angles of attack higher than  $5^\circ$  (Table 2). For low  $\alpha$  the error increases at 10%. The reason of this gap is caused by the hysteresis phenomenon: at low angle of attack the solution is not unique but two physical solutions exist and the URANS simulation converges on the second solution, the one for the decreasing  $\alpha$  [15]. Comparing the  $C_L$  value with the experimental hysteresis solution, the error reduces to less than 5% as at higher angles of attack. The skin friction comparison at  $\alpha=0^\circ$  shows the good agreement

between the oil flow visualisation and the numerical solution (Fig. 13). The laminar and turbulent zone are correctly detected on both the main and the flap element. The asymmetric separation on the wingspan is correctly reproduced even if with an overestimation of the separated zone near the main T.E.

**Table 2 –  $C_L$  comparison between experimental measurements and numerical simulations for  $\delta=25^\circ$ ,  $g/c_1=2.4\%$ .**

	WT	WT (hyst.)	URANS	$\Delta$ URANS / WT	$\Delta$ (URANS/WT (hyst.))
$\alpha=0^\circ$	1.25	1.07	1.12	-11.6%	+4.5%
$\alpha=2^\circ$	1.14	1.13	1.23	+7.3%	+8.1%
$\alpha=5^\circ$	1.24	1.16	1.24	0	+6.4%
$\alpha=8^\circ$	1.38	1.23	1.32	-4.5%	+6.8%
$\alpha=10^\circ$	1.27	1.13	1.33	+4.5%	+15.0%

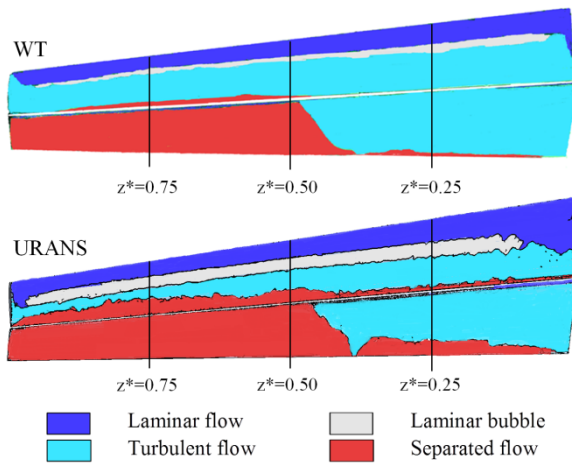


**Fig. 13 – Skin friction comparison between experimental viscous oil tests (top) and RANS simulation (bottom) for  $\delta=25^\circ$  and  $\alpha=0^\circ$ .**

### 3.3 Slot influence on the wing performance

The numerical approach was exploited to study additional slot configurations that were not possible to investigate experimentally.

The  $C_L$ - $\alpha$  curves for  $\delta=15^\circ$  case were reported in fig. 14 for the different slot configurations. The wing performance does not show significant improvements with the slot reduction. At  $\alpha=0^\circ$ ,  $C_L$  assumes the same value for the three slot configurations, with the main element that contributes to 2/3 of the global lift of the wing. Increasing the angle of attack, the medium slot size, i.e.  $g/c_1=1.6\%$ , appears to be the best one but with a gain of only 1.5% compared to the narrowest slot case. Increasing the angle of attack the main contribution increases linearly while the flap one rests constant as described by Rumsey et al. (2002) [16]. The separated zones on the wingsail surface at  $\alpha=0^\circ$  have similar extents at the three slot sizes. At  $\alpha=10^\circ$  the the slot

narrowing from  $g/c_1=2.4\%$  to  $g/c_1=1.6\%$  lead to an appreciable reduction of the separation zone while a further slot reduction does not introduce further significant modifications.

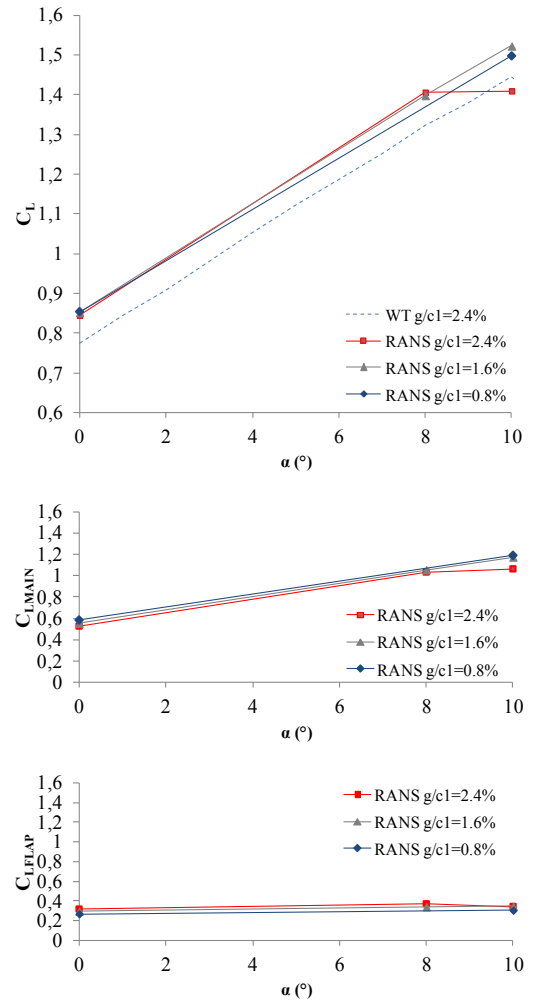


**Fig. 14 - Lift curves comparison for  $g/c_1=2.4\%$ ,  $g/c_1=1.6\%$  and  $g/c_1=0.8\%$  wingsail configurations at  $\delta=15^\circ$ .**

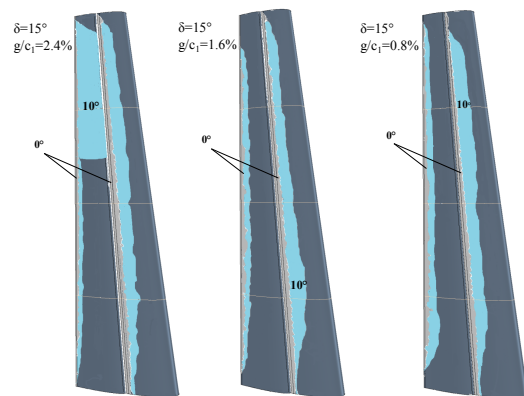


**Fig. 15 – Separated zones at different angles of attack for the wingsail configuration at  $g/c_1=2.4\%$ ,  $g/c_1=1.6\%$  and  $g/c_1=0.8\%$  for  $\delta=15^\circ$ .**

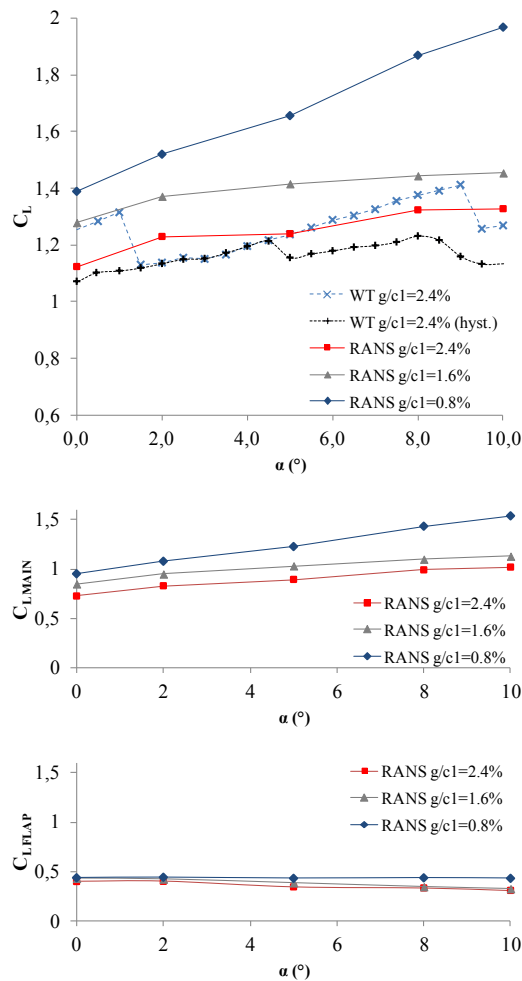


Fig. 16 - - Lift curves comparison for  $g/c_1=2.4\%$ ,  $g/c_1=1.6\%$  and  $g/c_1=0.8\%$  wingsail configurations at  $\delta=25^\circ$ .

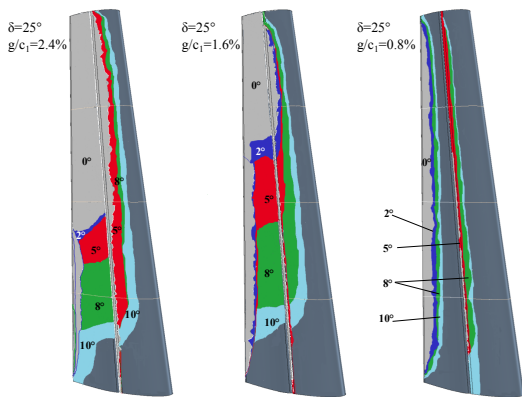


Fig. 17 – Separated zones at different angles of attack for the wingsail configuration at  $g/c_1=2.4\%$ ,  $g/c_1=1.6\%$  and  $g/c_1=0.8\%$  for  $\delta=25^\circ$ .

At  $\delta=25^\circ$  the wingsail performance in lift is more sensitive to the slot size (Fig. 16). The slot narrowing allows

increasing the lift coefficients for all the angles of attack with a gain up to 14% with the reduction from  $g/c_1=2.4\%$  to  $g/c_1=1.6\%$  and a gain up to 48% reducing the slot to  $g/c_1=0.8\%$ . The increase in lift is entirely due to the main element. This enhancement of the lift main effectiveness depends on the influence of the jet of the slot in modifying the velocity on the main T.E. altering the circulation on the main itself [3]. The  $C_L$  of the flap assumes same values in the three slot configurations at  $\alpha=0^\circ$  and tends to decrease with the increasing of the angle of attack. This decreasing is more and more elevated with the slot narrowing because of the strengthening of the main-flap interaction leading to a reduction in the pressure peak on the flap surface [3]. The reduction in pressure peak weakens the adverse pressure gradient on the flap surface and hence the probability of a flow separation. The reduction of the probability of a flow separation is also aided by the “off-surface pressure recovery” and “fresh boundary layer” effects described by Smith (1975) [3]. As it can be observed in fig. 17 the extension of the separated zones reduces by the narrowing of the slot at all the angles of attack. The evolution of the separation becomes also equally distributed throughout the wingspan.

The benefic effects introduced by the jet of the slot have not the same strength for all the slot size. The flow physics of the jet of the slot and its interaction with the flap boundary layer and main element wake is extremely sensitive to the slot size and only some optimal configuration allows enhancing sensibly the high lift performance of the wing. The benefic effects exist, as explained by Smith (1975) [3], only if the jet of the slot (potential flow does not merge with the neighboring viscous layers (i.e. the flap boundary layer and the main element wake). This aspect will be analyzed in the next section.

### 3.4 Flow layers profiles

The physics of the jet of the slot is highly influenced by the geometric slot parameters that modify the strength of the interaction with the neighbor flow layers and the possibility of a merging among them. The slot parameters for this section were reported in table 3 for the two cambered configurations and at the different slot size.

Table 3 –  $\alpha$  and  $y_F$  parameters for the two slot configurations at  $z^*=0.25$ .

	$\delta=15^\circ$		$\delta=25^\circ$	
	$g/c_1=0.8\%$	$g/c_1=2.4\%$	$g/c_1=0.8\%$	$g/c_1=2.4\%$
$\alpha/c_1$	-0.70	-2.44	-0.35	-1.98
$y_F/c_1$	1.53	1.99	2.49	3.25

The confluent boundary layer on the flap surface was investigated on both the high and low cambered wingsail configuration at the different slot size. The velocity profiles on the flap surface were carried out in order to investigate the merging characteristics of the flow. The profiles were extracted on two stations on the flap upper surface respectively at 5% and 10% of the flap chord, on the  $z^*=0.25$  section and at  $\alpha=0^\circ$ .

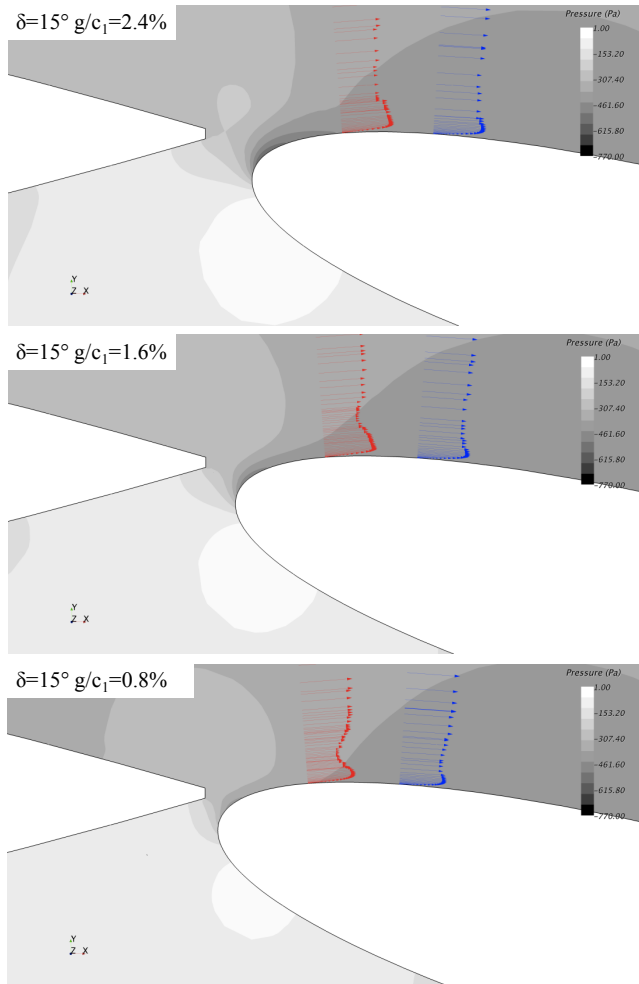


**Fig. 18** – Pressure scalar maps with streamlines on the slot region ( $z^*=0.25$ ) for  $\delta=15^\circ$ , at  $g/c_1=2.4\%$ ,  $g/c_1=1.6\%$  and  $g/c_1=0.8\%$ .

On the  $\delta=15^\circ$  the narrowest slot configuration shows a saturation of the slot jet (Fig. 18). The mass flow through the slot cannot correctly be dumped because of the reduced slot section. A recirculation zone appears on the main element lower surface near the T.E. to adjust the mass flow in the slot. The jet velocity is hence lower than in the wider slot configuration (Fig. 19). Nevertheless the narrowing of the slot improves the possibilities to keep unmerged the three flow layers. At  $g/c_1=0.8\%$  the layers merge at 10% of the flap chord but the strength of the jet velocity does not

change moving downstream in the flap surface. The merging is due to the main element wake velocity increase that evolves rapidly. This gain in velocity is enhanced with the slot reduction.

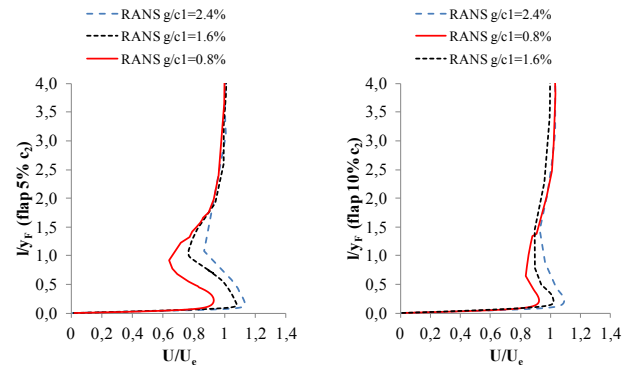


**Fig. 19** – **Fig. 21** – Comparison of the velocity profiles at  $g/c_1=2.4\%$ ,  $g/c_1=1.6\%$  and  $g/c_1=0.8\%$  for  $\delta=15^\circ$  at 5% and 10% of the flap chord ( $z^*=0.25$ ).

On the high cambered case the reduction of the slot size does not bring to jet saturation (the  $y_F$  is more elevated). The flow expands very quickly in its approaching to the slot throat. The expansion is due at first to the slot section reduction and in a second time to the flow contouring of the flap L.E. However in the narrowest slot case, the expansion for the section reduction continues until the neighbors of the flap L.E. preventing the second expansion due to the flap contouring. The pressure peak on the flap is hence smaller in magnitude compared to the wider slot. As a consequence of the lower expansion near the flap L.E., the recompression on the upper flap surface is slower and slower with the slot reduction. Hence the adverse pressure gradients are weaker, reducing the deceleration of the flap boundary layer and of the jet layer. In the downstream movement of the flow, the slot jet velocity remains constant for the narrowest slot configuration (Fig. 21).

The velocity profiles of the three slot configurations present similar shapes at 5% of the flap chord with the jet velocity decreasing with the narrowing of the slot size. At 10% $c_2$  the jet layer velocity assumes the same value for the three configurations. On this station, the  $g/c_1=2.4\%$  profile is completely merged while on the middle and narrow slot cases the different flow layers can still be distinguished. The more the jet tends to decelerate near the flap surface in the downstream movement the more the main wake layer velocity increases velocity causing the merging of the flow layers.

It can be noticed that the settings that introduce a strong enhancement in the lift capabilities of the wing ( $\delta=25^\circ$ ,

$g/c_1=0.8\%$ ) is also the setting preventing the merging of the flow layers on the flap.

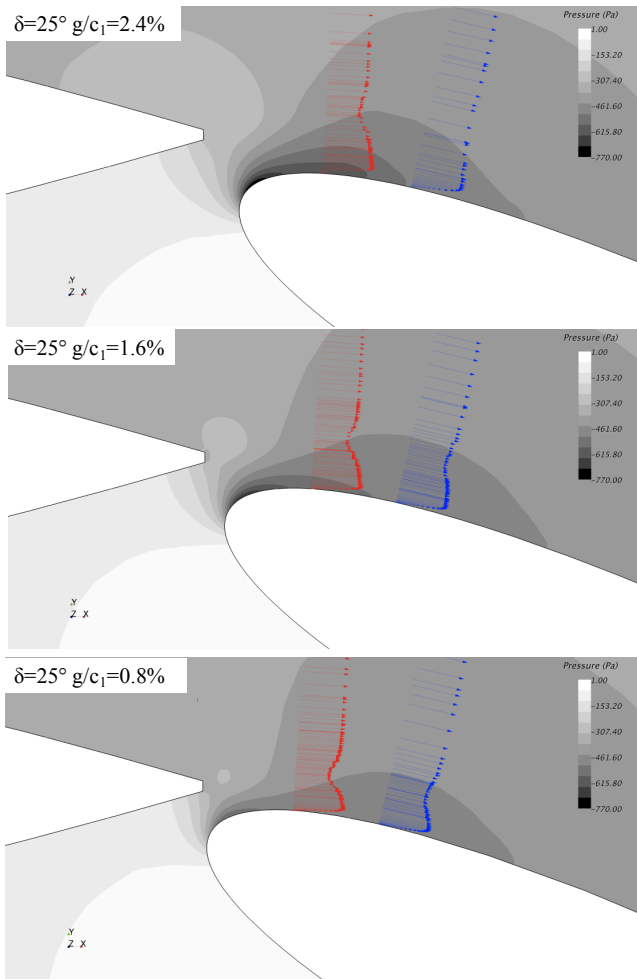


**Fig. 20** – Pressure scalar maps with streamlines on the slot region ( $z^*=0.25$ ) for  $\delta=25^\circ$ , at  $g/c_1=2.4\%$ ,  $g/c_1=1.6\%$  and  $g/c_1=0.8\%$ .

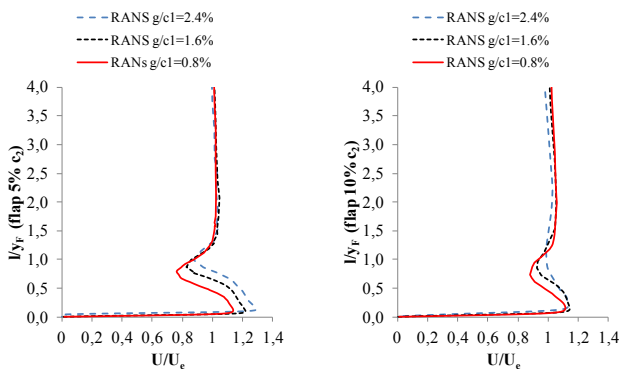


**Fig. 21** – Comparison of the velocity profiles at  $g/c_1=2.4\%$ ,  $g/c_1=1.6\%$  and  $g/c_1=0.8\%$  for  $\delta=25^\circ$  at 5% and 10% of the flap chord ( $z^*=0.25$ ).

The merging in the different cases is due to a reduction in the jet velocity and to an increase of the wake velocity.

Even if the flow layers are closest on the narrow slot configuration, it is in this case that the merging is retarded.

The jet layer is thicker on the wide configuration with a velocity that is more elevated than the narrow slot case. The mass flow here inside is more elevated with a consequent larger amount of jet flow momentum. The momentum is transferred to the wake layer by mean of the air viscosity increasing its velocity. The higher adverse pressure gradient in the wide slot case enhances the deceleration on the jet layer.

## Conclusions

An experimental campaign was performed on a wingsail scale model at two flap deflection angles (i.e.  $15^\circ$  and  $25^\circ$ ) modifying the slot size:  $g/c_1=2.4\%$ ,  $g/c_1=4.8\%$  and blocked slot.

In the  $g/c_1=2.4\%$  slot case, the low cambered lift curve has the classical linear increasing path with the angle of attack until the stall limit where the lift starts to decrease, gradually at first and abruptly finally. The flow separated from the wing surface in the same way on the entire wingspan and the same time on the flap and on the main element.

The high cambered configuration presents a fragmented path with four distinct stall points. Here the flow separates on the flap at first and on the main in a second time. The flap separation does not involve the entire flap surface at the same time but the mid-high section separates earlier than the lower ones.

The increase in the slot size spoils the lift performance of the wing in both the cambered settings. Nevertheless if at  $\delta=15^\circ$  the substantial effect is a decrease in  $C_{L,max}$ , at  $\delta=25^\circ$  the  $C_L$  has a large loss at all the angles of attack. The blocked slot configuration allows in turn an improvement of the lift performance at high angles of attack for the  $\delta=25^\circ$  case. On  $\delta=15^\circ$  settings the lift enhancements are lesser.

Numerical simulations were then performed on the scale model wingsail in the wind tunnel conditions. Wingsail was set at  $g/c_1=2.4\%$ ,  $g/c_1=1.6\%$ ,  $g/c_1=0.8\%$  and at both the flap deflection angles.

The slot reduction does not introduce sensibly improvements in the lift capabilities of the wing on the low cambered case. A limited increase in lift is observed. On the high cambered case the slot reduction lead to an increase in the lift capabilities of even 48% compared to the nominal case. The slot reduction acts on the evolution of the separated zones, reducing their extent and making the separation equally distributed throughout the wingspan.

The flow on the slot region was finally investigated on a section at  $z^*=0.25$  for the different wingsail settings. In the low cambered case, the confluent boundary layer on the flap surface is merged at the different slot sizes considered, preventing the possibilities to obtain the benefic effects of the jet of the slot described by Smith (1975) [3]. The  $g/c_1=0.8\%$  slot is also too narrow to dump all the mass flow. On the  $\delta=25^\circ$  case the reduction in the slot size reduces the probability of a merging of the flow layers of the flap surface enhancing the high lift capabilities of the wing. The merging is caused by the viscous interaction between the jet of the slot and the wake of the main. The more the jet mass flow the more is the shear stress with the main wake and hence the merging probability.

## References

- [1] Woodward, D.S., Lean, D.E. (1993), "Where is the High Lift Today? A Review of Past UK Research Programs", AGARD-CP-515, September 1993, Paper no 1.
- [2] Wentz, W.H., Fisco, K.A. (1978), "Pressure Distributions for the GA(W)-2 Airfoil with 20% Aileron, 25% Slotted Flap and 30% Fowler Flap", NASA Contractor Report 2948, Feb. 1978.
- [3] Smith, A.M.O. (1975), "High-Lift Aerodynamics", *J. of Aircraft*, 12(6), 501-530.
- [4] Turncock, S.R., Campbell, I.M., Magherini, M. (2014), "Parameters Affecting the Performance of the C-Class Wingsail", *Trans. RINA*, Vol 156, Part B1, IJSCT, 2014.
- [5] Blakeley, A.W., Flay, R.G.J., Furukawa, H., Richards, P.J. (2015), "Evaluation of Multi-Element Wingsail Aerodynamics form Two-dimensional Wind Tunnel Investigations", 5<sup>th</sup> High Performance Yacht Design Conference, Auckland, 10-12 March, 2015.
- [6] Haack, N., "C-Class Catamaran Wing Performance Optimization", Thesis for M.Phil., University of Manchester, 2011.
- [7] Chapin, V., Gourdain, N., Verdin, N., Fiumara, A., Senter, J. (2015), "Aerodynamic Study of a Two-Elements Wingsail for High Performance Multihull Yachts", 5<sup>th</sup> High Performance Yacht Design Conference, Auckland, 10-12 March, 2015.
- [8] Rogers, S.E., Roth, K., Nash, S.M. (2001), "Validation of Computed High Lift Flows with Significant Wind Tunnel Effects", *AIAA Journal*, vol. 39, No. 10, October 2001.
- [9] Nayani, S.N., William, L.S., Brynildsen, S.E., Everhart, J.L. (2015), "Numerical Study of the High-Speed Leg of a Wind Tunnel", 53<sup>rd</sup> AIAA Aerospace Science Meeting, Jan. 2015.
- [10] Fiumara, A., Gourdain, N., Chapin, V., Senter, J. (2015), "Comparison of wind tunnel and freestream conditions on the numerical predictions of a flow in a two element wingsail", 50<sup>th</sup> AAAF International Conference, Toulouse, 30 March – 1<sup>st</sup> April 2015.
- [11] Menter, F.R., Langtry, R.B., Likki, S.R., Suzen, Y.B., Huang, P.G., Völker, S. (2004), "A Correlation Cased Transition Model Using Local Variables – Part 1 –Model Formulation", *J. Turbomach* 128(3), 413-422, March 2004.
- [12] Menter, F.R., Langtry, R.B., Likki, S.R., Suzen, Y.B., Huang, P.G., Völker, S. (2004), "A Correlation Based Transition Model Using Local Variables – Part 2 –Test Cases and Industrial Application", *J. Turbomach* 128(3), 423-434, March 2004.
- [13] Suluksna, K., Dechaumphai, P., Juntasaro, E. (2009), "Correlations for Modeling Transitional Boundary Layers Under Influences of Freestream Turbulence and Pressure Gradient", *Int. J. of Heat and Fluid Flow*, 30(2009) 66-75.
- [14] Malan, P., Suluksna, K., Juntasaro, E. (2009), "Calibrating the  $\gamma$ -Re $\theta$  Transition Model for Commercial CFD", 47<sup>th</sup> AIAA Aerospace Science Meeting, Orlando, Florida, 5-8 Jan. 2009.
- [15] Kamenetskiy, D.S., Bussolletti, J. E., Hilmes, C.L., Venkatakrishnan, V., Wigton, L.B. (2014), "Numerical Evidence of Multiple Solutions for the Reynolds-Averaged Navier–Stokes Equations", *AIAA Journal*, Vol. 52, No 8, August 2014.
- [16] Rumsey, C.L., Ying, S.X. (2002), "Prediction of high lift: review of present CFD capability", *Progress in Aerospace Sciences*, 38 (2002) 145-180.